ROYAL SOCIETY OF CHEMISTRY

PAPER

Check for updates

Diffusion of bulky organic cations in the 3D/2D heterostructures to form interfacial quasi-2D (N2) phase for tin perovskite solar cells†

Ashank Seetharaman, [a] Sudhakar Narra, [ab] Parameswaran Rajamanickam, [c] Raghunath Putikam,[a] Ming-Chang Lin[a] and Eric Wei-Guang Diau [*ab]

The fabrication of a solution-processed multilayer (3D/quasi-2D/2D) heterostructure in tin perovskite is complicated and requires an orthogonal solvent system for the sequential layer deposition. Herein, we report the fabrication of multilayered heterojunction perovskite films by physically stacking 3D (E1) and 2D (N1) tin perovskite films with the aid of forceps-induced pressure or external light and heat stimulation. When applying the pressure by forceps or under external stimuli conditions, it would initiate a solid-phase transformation (SPT) to generate a stable new quasi-2D (N2) phase at the interface between 3D and 2D films with the linear chain-type organic cations (butylammonium (BA), hexylammonium (HA), and octyl ammonium (OA)). The mechanism behind the N2-phase formation can be understood as the diffusion of the bulky organic cations across the ion migration barriers to cut the 3D layer with appropriate ion exchange. In contrast, for the bulky aromatic organic cations, such as phenethylammonium (PEA), no SPT occurred to form the N2 phase with the forceps-induced prolonged storage, but the 0D phase can be produced under external stimuli light and heat exposure. Finally, using this approach, a prototypical solar cell device with an E1/N2/N1 configuration was fabricated, which gave a higher PCE (8.7%) than the pristine 3D device (PCE = 7.7%).

1 Introduction

Perovskite solar cells (PSCs) are progressively marching towards mass production owing to the pathbreaking power conversion efficiencies (PCE) attained from the devices of both single junction lead (Pb) PSC (25.8%) and silicon–Pb perovskite tandem solar cells (33.7%).[1,2] However, the toxicity of lead and the long-term stability of PSC (when compared with the silicon solar cells) are still challenging factors to overcome to meet the goals of the development of sustainable energy sources.[3] Among various alternatives to lead, tin (Sn)-PSC (TPSC) is emerging as a promising candidate with impressive PCE approaching 15%, despite the sensitive nature of Sn perovskites, which undergo degradation due to rapid Sn^{2+}/Sn^{4+} oxidation when exposed to air.[4,5] The success of improving the device performance and stability for TPSC can be attributed to the emerging lattice structural engineering methodologies, such as additive

engineering,[6–10] solvent-assisted engineering,[11–13] interfacial engineering,[14,15] surface passivation,[16,17] and formation of heterostructures.[18–27] Among these, three-dimensional (3D)/two-dimensional (2D) heterostructure formation has a distinct advantage of serving both as a protective barrier to prevent Sn^{2+}/Sn^{4+} oxidation and a charge-extraction layer between the perovskite and charge transporting layers to enhance the photovoltaic properties of the devices for TPSC. As a result, many efforts have been made to study such 3D/2D heterostructures for TPSC.[23–25,28]

Conventional solution-processed 3D/2D heterostructures formed *via* sequential deposition approaches using orthogonal solvents often produce gradient heterostructures as they would disturb the underlying layers during the fabrication of the top layers.[24] To overcome this problem, a simple physical pairing method that does not use solvents is desired. The concept of joining two perovskite solid films can be realized because of the soft ionic nature of the lattice surface that facilitates the diffusion of ions at the interface. The diffusion of halide ions across the physical barriers has been demonstrated between two interconnected Pb perovskite thin films.[29–31] Based on this idea, we coupled a 2D structure with a 3D structure using forceps so that bulky organic cations in the 2D structure can efficiently interact with the top surface of the 3D structure to form a 2D/3D heterostructure. A new quasi-2D phase was produced and stabilized at the interface as a result of the synergistic effect of

aDepartment of Applied Chemistry, Institute of Molecular Science, National Yang Ming Chiao Tung University, 1001 Ta-Hseuh Rd, Hsinchu 300093, Taiwan. E-mail: diau@nycu.edu.tw

bCenter for Emergent Functional Matter Science, National Yang Ming Chiao Tung University, 1001 Ta-Hseuh Rd, Hsinchu 300093, Taiwan

cDepartment of Materials Science and Engineering, National Yang Ming Chiao Tung University, 1001 Ta-Hseuh Rd, Hsinchu 300093, Taiwan

This journal is © The Royal Society of Chemistry 2023

J. Mater. Chem. A, 2023, **11**, 21089–21098 | **21089**

interfacial destruction and ion migration in both films, generating a multilayered perovskite system. The interactions of bulky organic cations in the 2D structure with the Frenkel and Schottky types of defects on the surface of the 3D lattice are crucial in the formation of interfacial phases due to ion migration. For example, for the 2D structure employing linear alkyl ammonium cations, *e.g.*, butylammonium (BA), hexylammonium (HA), octylammonium (OA), and so on, may lead to deep penetration of the cations into the 3D lattice structure, effectively stitching the films through the interfacial layer growth of the quasi-2D phase, whereas employing bulky aromatic organic cations, *e.g.*, phenethylammonium (PEA), may develop localized contact and prevent the diffusion of ions due to varied steric and electronic interactions. The mechanism of halide ion diffusion is well known,[31–35] however, the mechanism of bulky organic cation diffusion in the interface of a 3D/2D heterostructure has not been reported.

In the present study, we fabricated four 2D (N1) Sn perovskite thin films ($n = 1$, L_2SnI_4; L = BA, HA, OA or PEA) and combined them with the 3D (E1) Sn perovskite thin film (FASnI$_3$ + 1% EDAI$_2$; EDA represents ethylenediammonium) using forceps-induced pressure or external heat and light as a driving force. We found that solid-phase transformation with the former driving force occurred to grow the 2D-N2 phase ($n = 2$, $L_2FASn_2I_7$) only for the linear bulky organic cations (BA, HA, and OA) in the interface between the N1 and E1 films at room temperature. In contrast, under light-soaking and thermal-stress conditions, complete formation of the N2 phase was observed for BA, HA, and OA cations, but only partial formation of the N2 phase occurred for the PEA cation. After storage for four days, the forceps-pressed sample was split into two parts, the E1N1/E1 part was fabricated to a solar cell with a triple

active layer (E1/N2/N1) to attain PCE 8.7%, which is superior to the pristine E1 cell (PCE 7.7%) fabricated under the same experimental conditions. This work not only provides a simple physical stacking approach to fabricate a triple active layer tin perovskite solar cell with decent performance but also gives an in-depth mechanistic understanding of the solid-phase transformation process in tin perovskite heterostructures.

2 Results and discussion

2.1 Forceps-assisted physical stacking procedure

The schematic demonstration of the stacking process is illustrated in Fig. 1. Briefly, 3D (E1) and 2D (N1) perovskite films with different bulky organic cations were spin-coated on separate glass substrates and annealed at 70 °C for 10 min. As soon as the annealing was over, the corresponding 3D and 2D films were stacked atop each other using forceps-induced pressure for 10 min and encapsulated, then the forceps was removed. For reference, pristine E1, N1, and N2 samples with different bulky organic cations were also prepared similarly. The scanning electron micrograph (SEM) and X-ray diffraction (XRD) patterns of the pristine (reference) samples are shown in Fig. S1 and S2,† respectively. The structural changes in the stacked E1N1 (L = BA, HA, OA, or PEA for the N1 case) films were monitored using various spectral techniques for a period of one month. The absorption spectra (Fig. S3†) of both pristine E1 and N1 films displayed bands corresponding to free carrier absorption and excitons. In contrast, E1N1 samples showed temporal growth of the N2 phase at the expense of the pristine N1 and E1 phases (Fig. S4†) for BA, HA and OA samples; there was no spectral change for the PEA sample after aging for 30 days.
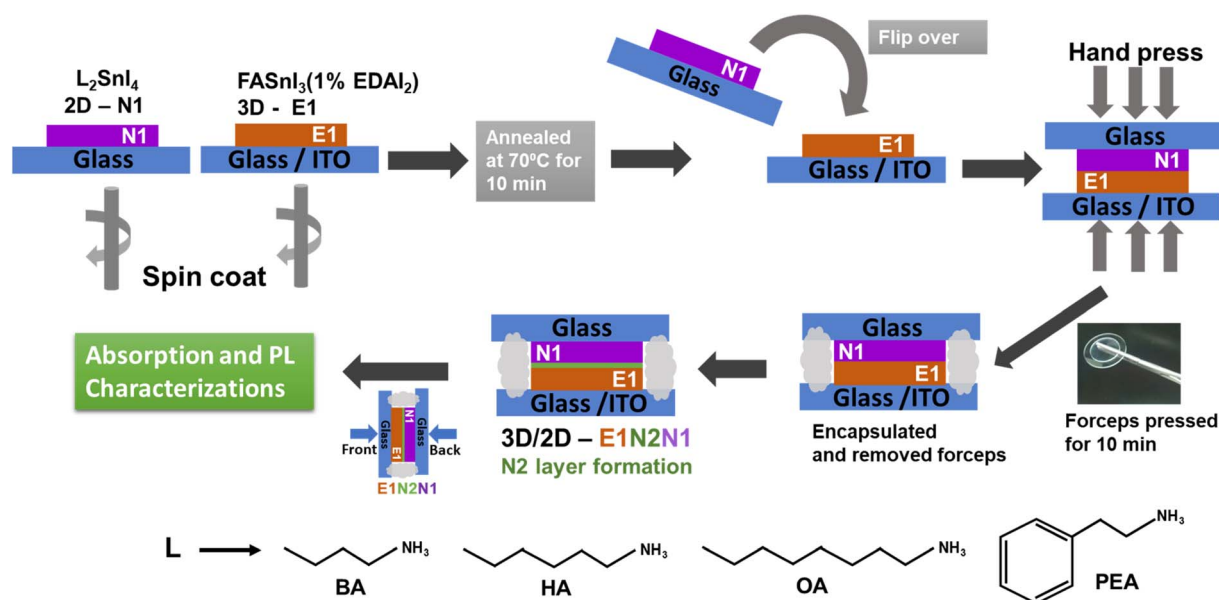

Fig. 1 Schematic demonstration of stacking process to form a 3D/2D Sn perovskite heterostructures. Two thin films (N1 and E1) were spin-coated separately and stacked on top of each other using forceps for 10 minutes, then encapsulated, removed the forceps, and stored in the dark at room temperature for periods of 1 to 30 days. Steady-state absorption and photoluminescence spectral measurements were performed at varied periods of storage.

21090 | *J. Mater. Chem. A*, 2023, **11**, 21089–21098

This journal is © The Royal Society of Chemistry 2023

2.2 PL spectral evolutions for excitation from the front (E1) and back (N1) sides

The photoluminescence (PL) spectra of the E1N1 samples were measured by excitation from both the front (E1) and back (N1) faces of the stacked films under two conditions (Fig. 2): (1) continuous storage in the dry box maintained at a relative humidity (RH) of 50% for 30 days (referred as aging effect) and (2) continuous illumination under one sun condition with the samples heating at 50 °C for 48 hours (referred to as the external effect). The prolonged storage sheds light on the cumulative effects of the compressive and tensile strains on the electronic structural changes of the E1N1 samples whereas the external effect helps us to track the rate of diffusion of ions and robustness of the samples based on the molecular structure of the spacer cation. Fig. 2a and b show the PL spectra of the E1N1 samples aged for 1 and 30 days, whereas Fig. 2c and d show the PL spectra at initial (0 h) and final (48 h except 10 h for PEA) durations under the applied light-soaking and thermal-stress conditions for the frontside and backside excitations, respectively. The PL spectral changes during the intermediate stages of aging and external effects are shown in Fig. S6 and S12,† respectively. Excitation from the front side (E1) allows us to monitor the electronic structural changes in the bulk (thicker) 3D phase while the backside excitation from the thinner 2D sheet (N1) offers us the advantage to monitor the PL signals from both 2D and 3D phases together with the newly formed interfacial N2 phases.

Frontside excitation of E1N1 samples showed modest changes in the spectral shapes and positions due to aging between the spectra recorded for day 1 and day 30 as shown in Fig. 2a, whereas external stimuli produced large shifts between 0 h and 48 h spectra due to the formation of new phases such as N2 and quasi 2D phases, as shown in Fig. 2c. As mentioned above, the backside excitation of E1N1 samples (Fig. 2b and d) showed signals from N1, E1, and the newly formed interfacial N2 phase due to the diffusion of the organic cations from both 2D and 3D sides. It can be seen that both aging (Fig. 2b) and external (Fig. 2d) effects showed the N2 phase as one of the prominent final phases of the reaction between the coupled 3D and 2D samples, except for the case of bulky aromatic PEA cation.

To confirm the presence of the N2 phase as well as evaluate its carrier dynamics in the E1N1, the femtosecond transient absorption spectral (fs-TAS) studies were performed for E1N1-BA (day 4). The fs-TAS of the intact E1N1-BA films in comparison with pristine E1, N1, and N2 samples using a 620 nm actinic pump pulse as the excitation source and was probed in the region between 550–990 nm, as shown in Fig. S7a.† To better visualize the presence of N2 phase, the 2 ps TAS profile of all samples were compared, as shown in Fig. 3. The TAS profiles of pristine N1 and N2 samples showed photo-bleach (PB) signals of their respective excitonic states, whereas the pristine E1 sample showed PB bands due to the depletion of band edge states caused by carriers. The physical significance of PB and the photo-induced absorption (PIA) bands in the pristine
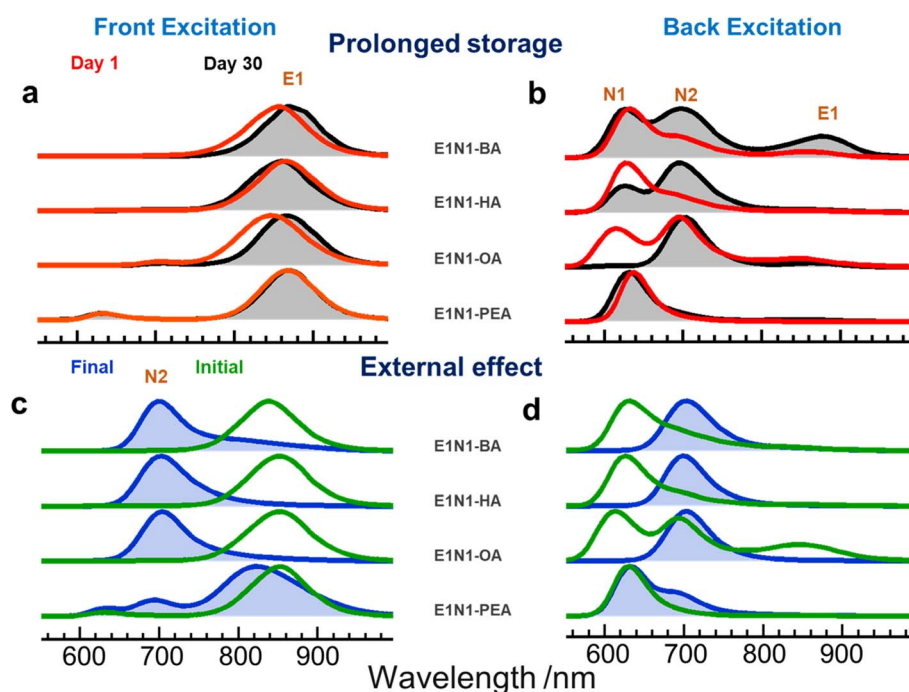

Fig. 2 Photoluminescence (PL) spectra of the stacked thin-film samples to demonstrate the evolution of the N2 phase. (a) and (b) show normalized PL spectra for the stacked film (E1N1) with excitations from the front (E1) and the back (N1) sides, respectively, for the fresh and aged samples as indicated. (c) and (d) show normalized PL spectra for the stacked film (E1N1) with excitations from the front (E1) and the back (N1) sides, respectively, under external effect (illumination at one sun and heating at 50 °C). The initial and final states represent the PL spectra before the initiation of external effect and after rapid phase conversion to the N2 phase, respectively.
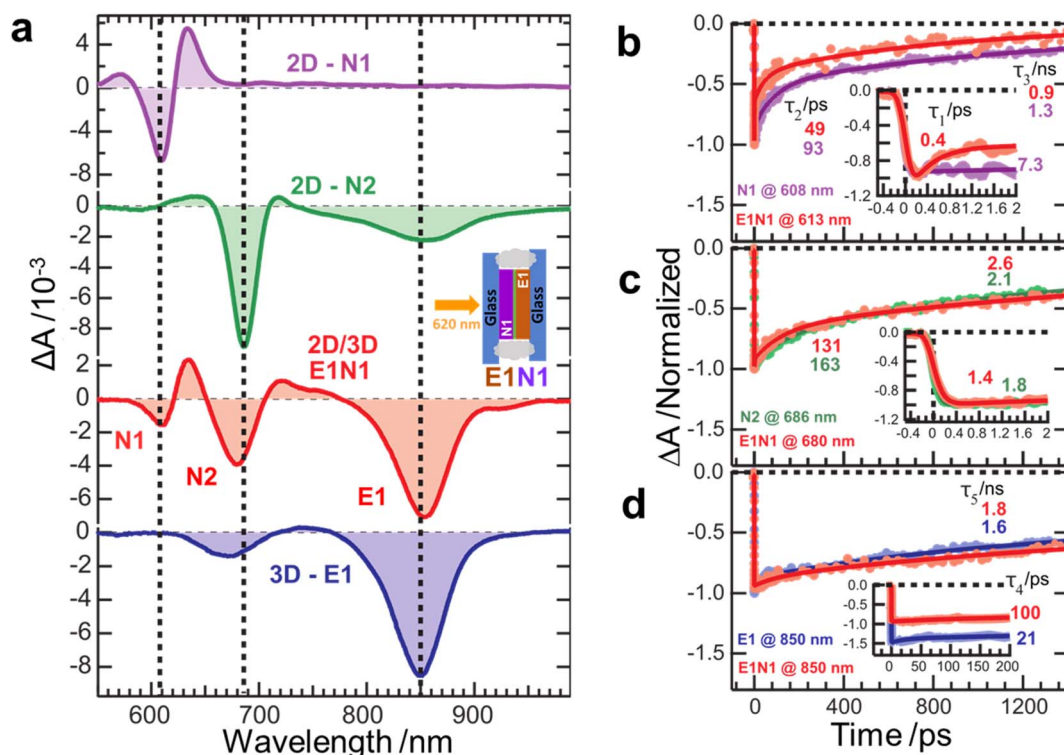
This journal is © The Royal Society of Chemistry 2023

J. Mater. Chem. A, 2023, **11**, 21089–21098 | **21091**

Fig. 3 Time-resolved spectral characterizations of E1N1-BA (day 4) obtained from fs-TAS measurements with the excitation at 620 nm. (a) Femtosecond (fs)-TAS spectral trace at 2 ps delay times for N1, N2, E1N1, and E1. (b)–(d) fs-TAS temporal profiles for pristine and E1N1 samples at photo-bleach (PB) band positions. The fitted time coefficients are indicated as τ_1/ps, τ_2/ps, τ_3/ns, τ_4/ps, and τ_5/ns.

samples have been reported in detail elsewhere.[36,37] Interestingly, the probed E1N1 sample displayed signals associated with those of the pristine samples: N1, N2, and E1. It is important to note that the 680 nm PB band in the E1N1 film had spectral overlaps from both of the PB bands of E1 and N2, however, its strong intensity and narrow bandwidth resembled those of N2. Therefore, a clear assignment of the 680 nm PB band for the E1N1 film was sought by selective excitations using 680 and 780 nm excitation pulses, as shown in Fig. S8–S11.† Resonant excitation (680 nm) produced a much sharper and more intense PB band resembling that of pristine N2 (Fig. S9†) whereas near band edge excitation (780 nm) of E1 produced PB bands at 680 nm resembling that of E1 (Fig. S11†). Thus, the observation of the 680 nm band under 620 nm excitation can be used as evidence for the formation of N2 at the N1/E1 interface.

The TA kinetics of 2D (N1, N2) and 3D (E1) samples manifested the relaxation dynamics of excitons and carriers, respectively, as described elsewhere.[36,37] Thus, a relative comparison of decay features between pristine and E1N1 samples revealed the splitting of excitons and charge separation at the interfaces between E1 and N1. The observed decay profiles were simulated by fitting them with an appropriate number of exponential decay functions, as indicated by time coefficients in Fig. 3b–d. The PB band of N1 in the E1N1 film showed drastic quenching ($\tau_1 = 0.4$ vs. 7.3 ps in pristine N1) due to the splitting of excitons at the interface between N1 and N2. The band alignment between the N1, N2, and E1 (Fig. S7b and S18c†) favoured hole migration from the 2D to 3D phase, thus

the drastic quenching with a time constant of 0.4 ps observed for the PB band of N1 in the E1N1 film could be due to rapid hole injection from N1 to N2 at the interface. The ps–ns decaying components of N1 in the E1N1 film also showed faster recombination compared with the pristine N1 sample ($\tau_2 = 49$ vs. 93 ps, and $\tau_3 = 0.9$ vs. 1.3 ns) due to the formation of interfacial trap states. These findings suggest that there is a significant amount of traps in N1 due to lattice strain caused by stacking and trap formation as a result of interfacial layer formation.

The PB band of N2 in E1N1 (Fig. 3c) showed only a slight quenching effect compared with N1 ($\tau_1 = 1.4$ vs. 1.8 ps and $\tau_2 = 131$ vs. 163 ps), probably due to the contamination of N2 with higher-order 2D structures so that the spectral overlap of the PB band of N2 with that of E1 became significant. Finally, the PB band of E1 in E1N1 (Fig. 3d) showed slow relaxation (τ_4 and τ_5) compared with that of pristine E1 due to hole migration from N1 and surface passivation offered by the alkyl chains. A relaxation scheme describing the key carrier relaxation pathways of E1N1 film is shown in Fig. S7b.†

The aging experiments suggest that the effects of strain are nominal on the bulk 3D phases with the interfacial N2 phase being localized to a few surface layers with a time-dependent growth, as shown in Fig. S6.† The red spectral shifts in the 3D phases due to aging can be attributed to the modulation in the electronic structures caused by the structural rearrangement of ions due to the formation of the N2 phase at the interface. The time-dependent growth of the N2 phase indicates the slow

21092 | J. Mater. Chem. A, 2023, **11**, 21089–21098

This journal is © The Royal Society of Chemistry 2023

diffusion of organic cations with time. Among the bulky organic cations, PEA showed no N2 phase formation together with the negligible effects of aging whereas OA showed complete consumption of the N1 layer to form the N2 phase. The latter is due to the thinner film formation because of the poorer solubility of the OA precursor solution. The absence of the N2 phase at the interface between 3D and 2D-PEA layers could be either due to a large ion migration barrier hindering the diffusion of PEA cations or the molecular size of PEA, which is too bulky to penetrate into the 3D phase when compared with the linear alkyl chain cations.

The external stimuli experiments showed that the samples with linear alkyl chains (BA, HA, and OA) were completely changed into the N2 phase (Fig. S12a–c†) while the PEA sample displayed weaker N2 phase, as shown in Fig. S12d.† Further, the E1 bands showed significant blueshifts in all samples due to the formation of low-dimensional phases with a decrease in the intensity of E1 band maxima, as shown in Fig. S13† (also in Fig. S14a and b† for the PEA case). The externally applied heat and light-illumination expedited the diffusion of organic cations by surpassing the necessary ion migration barrier (lower activation energy) as shown by the incremental growth of the N2 phases with time in Fig. S12.† The ions' lower activation energy might weaken the metal halide bond, resulting in lattice strain.[38–42] This softens the perovskite lattice, which can aggravate the ion migration. As a result, when exposed to external stimuli, the physically stacked films soften and pair more efficiently. The molecular interaction at the interface is also improved, allowing ions from the film to migrate more easily under external stimuli (light and heat).

The rates of diffusion of organic cations were attained by monitoring PL intensity variations of both the E1 (860 nm) and N2 (698 nm) bands. The decrease of E1 bands shows time coefficients of 218, 203, 240, and 185 min for BA, HA, OA, and PEA cations (Fig. S13†). Similarly, the formation of N2 bands shows slightly slower rising coefficients than their E1 bands, with values of 456 and 329 min for BA and PEA cations, respectively (Fig. S13†). The N2 band intensities of the HA and OA samples showed a scattered behaviour and thus were not fitted to attain the formation time coefficients. The slower formation of the N2 phases compared to the disappearance of the E1 phase suggests that the N2 phase is formed via the higher-order low-dimensional phases (N_x, $x > 2$). Furthermore, for the linear alkyl chain cations (BA, HA, and OA), the N1 and E1 phases were converted completely into the N2 phase (Fig. 2c, d and S12†). In contrast, the bulky aromatic cation PEA showed only partial conversion to the N2 phase at an irradiation time of 10 h. Beyond this irradiation period (e.g., 700 min), the sample might turn to a zero-dimensional (0D) phase, as shown by its absorption and PL spectra in Fig. S14c.† It should be noted that our observation is consistent with the UV-Vis absorption spectra of the 0D tin bromide perovskites reported elsewhere.[43,44] The formation of a 0D phase for the PEA cation indicates that diffusion of bulky organic cations disrupts the inorganic lattice leading to the formation of hollow structures with larger voids initially, and then producing the 0D phases as observed herein.

The observed PL spectra (ageing) showing the formation of the interfacial N2 phase should be due to the diffusion of the linear bulky organic cations (BA, HA, and OA) from either the microcracks developed during the initial contact between N1 and E1 samples or the cumulative effects of compressive and tensile strains caused by the application of forceps-induced pressure. Either of these processes can distort the lattices at the interface between N1 and E1 phases to release the organic cations and iodide anions. Hence, a large number of voids will be generated to provide a channel for the rearrangement of these ions from both sides of the stacked film. Once N2 formation is initiated, it grows further by consuming E1 and N1 lattice structures due to the reoccurrence of microcracks caused by the sustained forceps-induced pressure. The effects of heat and light can further aggravate the diffusion process by supplying additional energy to attain a stable low-dimension phase. However, PEA could not form the N2 phase without the aid of external energy such as heat and light, and this suggests that bulky PEA molecules are robust and do not induce any additional low-dimensional phases as they need external stimuli to overcome the ion migration barrier for diffusion, but once diffused it will lead to 0D phase.

We now consider E1N1-BA as an example. When E1 is pressed against N1, the surface of E1 can undergo lattice distortions. Due to this effect, a series of surface SnI_6^{4-} octahedral units can stretch outwards, causing it to tilt slightly so that FA, BA cations, and iodine anions can move outward. This makes the surface more amorphous, which can be better visualized by measuring the X-ray diffraction (XRD) patterns of the half-split E1N1-BA stacked film over varied storage periods (Fig. 4a). The schematic demonstration of the film stacking and splitting processes are shown in Fig. S15.† When the stacked E1N1-BA film was apart, it formed two films, named as E1N1/E1 (E1 side) and E1N1/N1 (N1 side). The XRD patterns of the E1N1/E1 and E1N1/N1 films are compared with those of the pristine E1, N1, and N2 films, as shown in the bottom of Fig. 4a. The (h,k,l) index values are assigned based on those reported elsewhere.[6,36]

2.3 Mechanisms for the formation of the N2 phase with the BA cation and the formation of the 0D phase with the PEA cation

The XRD patterns of the E1N1/E1(BA) film on day 4 clearly showed prominent peaks of the N1 (6.4°) and E1 (14.0°) phases together with a weak N2 peak located at 4.4°. The peaks shifted toward smaller angles in XRD, confirming the electronic structural changes caused by the formation of the quasi-2D phases, whereas band broadening and shoulders in XRD confirmed the loss of crystallinity (amorphization, tensile strain) at the interface due to microcrack formation. In contrast, the XRD patterns of the E1N1/N1(BA) film showed only the strong N1 peak at 6.4° together with a weak N2 peak at 4.6°. Furthermore, the N1 peaks of the E1N1/E1(BA) sample observed on day 4 disappeared on day 15 and day 30, indicating that the interfacial N1 phase was completely transformed to the N2 phase on the split E1N1/E1(BA) film. This was validated by the

This journal is © The Royal Society of Chemistry 2023

J. Mater. Chem. A, 2023, **11**, 21089–21098 | **21093**

Fig. 4 Structural characterization of pristine and split opened E1N1-BA heterostructures. (a) XRD patterns are shown for split opened E1N1/E1 and E1N1/N1 (day 4, 15 and 30) films in varied storage periods to compare with those of the pristine E1, N1, and N2 films shown at the bottom of the figure. The dotted lines indicate the major peaks positions for the E1, N1, and N2 films as indicated. (b) SEM images of pristine E1, N1, and split opened E1N1/E1 and E1N1/N1 samples under varied storage periods (day 4, 15, and 30).

scanning electron micrograph (SEM) studies, which revealed the presence of N1 and N2 on E1. Fig. 4b shows the SEM images for the split opened sample on days 4 to 30 from both E1 and N1 sides. In comparison to the pristine E1, the surface morphology on the day 4 sample had a N1-like nanosheet structure along with the surface grain distribution of the 3D structure underneath. The day 15 split opened sample, on the other hand, had complete coverage of grain boundaries with a N2 sheet-like structure above the E1 3D structure. The day 30 split opened samples had similar morphology with no significant difference with the day 15 sample.

To gain more insight into the development of the N2 phase, we can describe the interaction between N1 and E1 stoichiometrically using eqn (1):

$$L_2SnI_4 \text{ (N1)} + FASnI_3 \text{ (E1)} \rightarrow L_2FASn_2I_7 \text{ (N2)} \quad (1)$$

Here, L is either one of the BA, HA, and OA cations; for the PEA cation, no N2 phase was observed under the aging condition.

A mechanistic demonstration of the formation of the N2 phase via the interaction of N1 with E1 for the linear cation

samples is shown in Fig. 5a. Initially, the lattice distortion and micro cracking in the N1/E1 interface occurred via the forceps-induced pressure to release L, FA cations, and iodide anions. Then, two L cations moved to the FA position in the distorted E1 lattice to cut one layer of E1 and create an iodine vacancy to be occupied by the iodine anion released from the N1 layer; simultaneously, one interfacial FA cation could move to the L vacancy and this ion exchange process repeated to form one, two, three, and more layers of the N2 phase, as shown in Fig. 5a. Note that the aforementioned mechanism is for an ideal case, and some higher-order 2D phases should also be produced via a similar ion exchange mechanism, however, eventually, N2 would remain the dominant phase to stay.

Alternatively, the N2 phase can also be produced by consuming two N1 units with FAI from the E1 phase and releasing two LI from the N1 phase according to eqn (2):

$$2L_2SnI_4 \text{ (N1)} + FAI \text{ (from E1)} - 2LI \text{ (from N1)} \rightarrow$$
$$L_2FASn_2I_7 \text{ (N2)} \quad (2)$$

21094 | J. Mater. Chem. A, 2023, 11, 21089–21098

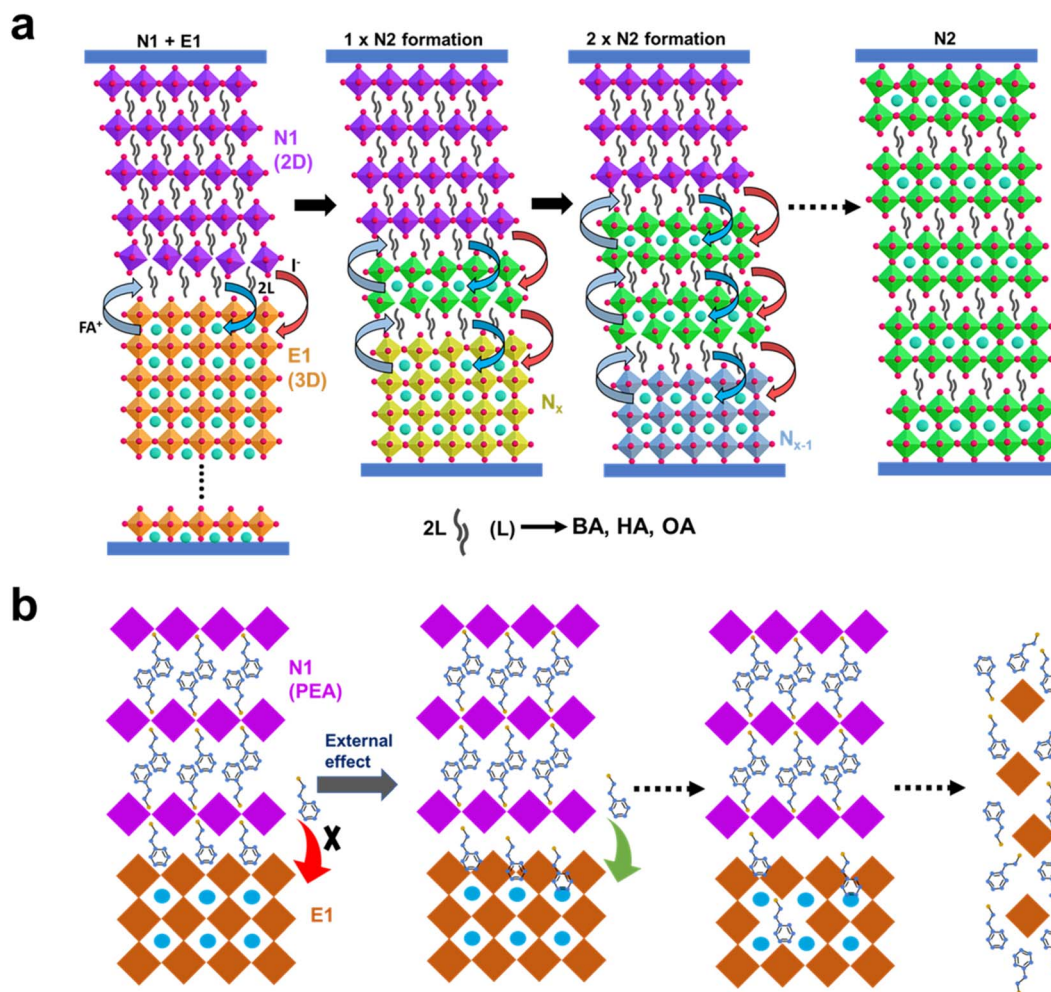This journal is © The Royal Society of Chemistry 2023

Fig. 5 Mechanistic demonstration showing (a) the formation of N2 phase at the E1/N1 interface for BA, HA and OA cations under aging condition and (b) the formation of 0D phase tin perovskite for the PEA cation under external stimuli condition. N_x denotes higher order 2D phases.

Herein, we consider the ion exchange to occur with the L cation in the second layer of N1 so that it produces the E1/N1/N2/N1 configuration and eventually it would produce more N2 layers when the ion exchange proceeds. On the other hand, the N1 phase with PEA as a bulky aromatic ligand cannot convert into the N2 phase under the aging condition due to the steric hindrance effect of the bulky PEA cation with greater ion migration barrier than the linear bulky organic cations. However, under the light-soaking and heat-stress conditions, PEA gained sufficient energy to overcome the ion migration barrier and moved out to the E1 crystal to make it a hollow structure, and eventually a 0D phase would be produced as shown in Fig. 5b. The mechanism would be similar under external stimuli, except that the rate of the solid-state reaction would increase.

2.4 Why did the N2 phase became dominant according to eqn (1) and (2)?

To answer this question, we performed Density Functional Theory (DFT) calculations using VASP software to estimate the formation energies of the 2D perovskites with barrier lengths

(BA) ranging from $n = 1$ to 6 (N1–N6). The optimized geometries for 3D, N1, 3D/N1, and 3D/N2/N1 are shown in Fig. S16,† and the corresponding lattice parameters are listed in Table S1.† As shown in Fig. S17a and b,† N1–N6 structures were optimized without and with the BA chains. For the slabs without BA chains, the formation energies decrease exponentially from N1 to N6 (Fig. S17c†). It was reported that the formation of N1 is energy intensive and the formation of higher-order phases is more likely in the presence of larger amounts of cations.[45,46] Our calculations on slabs in the absence of BA chains well agreed with the results reported elsewhere,[45,46] indicating that the formation of N1 is indeed an energy-intensive process to produce, and the N2 slab is more stable than the N1 slab by ~ 1.5 eV. In other words, in an extreme case when all the BA chains are removed, N1 is very unstable compared to N2 and other higher order 2D phases (Fig. S17c†). However, the estimated formation energies increase as the barrier length increases from N1 to N5 (product phases) in the presence of BA chains (Fig. S17d†).

Our results show that N2 is the dominant low-dimensional phase in the heterostructure. Both E1 and N1 are reactant

This journal is © The Royal Society of Chemistry 2023

J. Mater. Chem. A, 2023, 11, 21089–21098 | 21095

states, as shown in eqn (1) and (2). Our product states include all states from N2 to the higher order N_x phase. Dangling bonds established on one or both sides of N1 and E1 cause ion movement. As a result, new phases emerge, with N2 being the most stable product phase according to our calculations, neglecting the stability of the reactant N1. It is nearly impossible to convert the majority of the E1 to the N1 phase because we cannot entirely move the FA cations out of the system. They have to be accommodated inside the lattice. In such a scenario, the complete transformation of the bulk to the N2 phase is a more plausible reaction path than turning it back to the N1 phase. Based on our experimental observations, the phase transformation from N2 to N1 should involve a high energy barrier that prevents the back reaction from occurring.

2.5 A tin-based perovskite solar cell fabricated with E1/N2/N1 triple active layers

As the XRD patterns shown in Fig. 4, E1N1/E1 films of day 4 and day 15 conditions were used to fabricate a tin perovskite solar cell with the device configuration of ITO/PEDOT:PSS/E1/N2/N1/C_{60}/BCP/Ag, as shown in Fig. 6a; the corresponding energy-level diagram is shown in Fig. 6b (the valence and the conduction band (VB and CB) levels were estimated using UPS data shown in Fig. S18a† and bandgap values obtained from PL peak maxima shown in Fig. S18b†). Note that the active perovskite layer contains three components (E1/N2/N1) on day 4, whereas, it contains only two components (E1/N2) on day 15. The characteristic J–V curves and the corresponding IPCE spectra are

shown in Fig. 6c and d, respectively; the corresponding photovoltaic (PV) parameters are given in Table S2.† As a result, the day 4 device attained J_{SC}/mA cm^{-2} = 23.7, V_{oc}/V = 0.50, FF = 0.73, giving a total PCE of 8.7%, which outperforms that of the reference device made of the pristine E1 layer (PCE 7.7%). For the 15-day device, it gave a poorer PCE (6.1%) than the others, because the E1/N2 layer was unfavourable for electron transfer due to the higher barrier of the thicker N2 layer. Note that there was no effect of hysteresis for all the devices studied herein. Furthermore, the greater V_{oc} observed on day 4 might be due to the large bandgap of N1 nanosheets and the weak N2 phase formation. The device made on day 15, on the other hand, features a thicker N2 phase, which could have band-bending interaction with E1, causing electronic band structural changes in E1 that results in trap states and significant charge recombination. Both of these factors contribute to the decreased V_{oc} and poorer PV performance for the E1/N2 device than for the E1/N2/N1 device.

Although the device performance is moderate, this is the first report on the TPSCs with triple active layers containing 3D, N2, and N1 phases in an energy cascade configuration, as shown in Fig. 6b. Even though the CB levels of the N2 and N1 layers are slightly higher than that of E1 layer, band alignment should occur for the electrons in the CB of E1 to successfully transfer to the CB of C_{60} to attain decent J_{SC} values for both, day 4 and day 15 devices. We summarize in Table S3† all the device performances of TPSC with 3D/2D architectures reported in the literature for comparison.
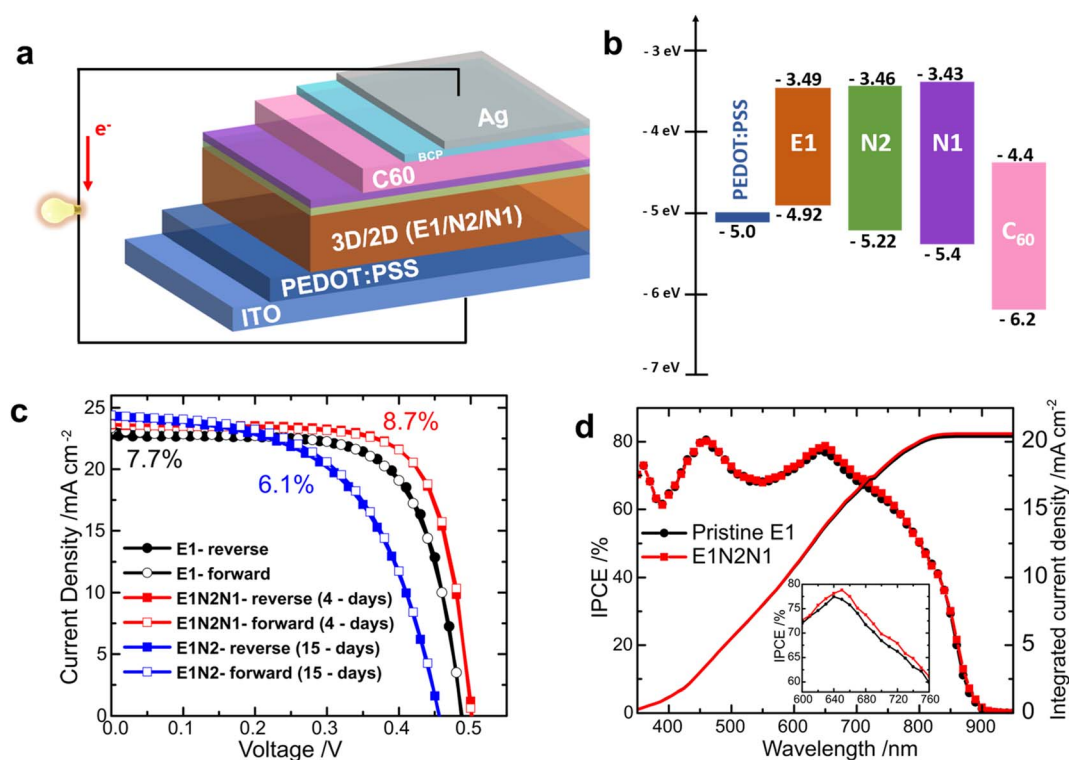

Fig. 6 Device structure and performance for the tin perovskite solar cells using the E1N1/E1 substrate. (a) Device architecture, (b) energy-level diagram of the corresponding layers, (c) J–V characteristic curves for the devices as indicated, and (d) corresponding IPCE spectra for pristine E1 and triple active layer (E1/N2/N1) devices.

21096 | J. Mater. Chem. A, 2023, 11, 21089–21098

This journal is © The Royal Society of Chemistry 2023

3   Conclusions

We constructed a 3D/2D heterostructure by physically stacking the 3D (E1) and 2D (N1) Sn perovskite samples (E1N1) using forceps. When the E1 and N1 films are contacted with each other at room temperature, structural distortions, and ion migrations occur, causing the formation of a new N2 phase between the E1 and N1 phases. The formation of the N2 phase at the interface was further confirmed by fs-TAS and carrier relaxation dynamics for each phase. Bulky linear organic cations such as BA, HA, and OA can effectively create the interfacial N2 phase, whereas bulky aromatic cations such as PEA cannot form the interfacial N2 phase under aging conditions, however, PEA can lead to the formation of the zero-dimensional phase under external light-soaking and thermal-stress condition. Long-term stacking of films allows linear cations to penetrate deeply into the lattice structure, causing structural deformation. As a result, the recurrence of structural distortions, as well as ion migrations at newly formed interfaces, ensures the growth of the new N2 phase as the storage duration increases. The process of such interfacial development is due to disrupted crystallinity in the interface, which allows one FA and two L (BA, HA, and OA) cations to exchange with proper migration of the iodine anions to occupy the iodine vacancies created by the L cations to cut the E1 layers. Furthermore, this interfacial ion migration process is continuous until the entire stacked sample is completely converted to the N2 phase with formation energy lower than the others predicted by density functional theory and supported by both PL and XRD characterizations. Finally, after four days of stacking, a triple-layer tin perovskite (E1/N2/N1) was produced on the E1 side of the split E1N1 substrate. This triple-layer tin perovskite was fabricated into a solar cell to attain a PCE of 8.7%, which is greater than the pristine E1 device (PCE 7.7%) fabricated under the same experimental conditions.

4   Experimental

Details of thin film fabrication, mechanical stacking methodology, solar cell device fabrication, computational (DFT) calculations, and supporting photophysical and structural characterizations are included in ESI.†

Author contributions

Conceptualization: A. S., S. N., and E. W.-G. D. Methodology: A. S. Film fabrication, optical characterization (UV-Vis, PL, fs-TAS), SEM, XRD, and UPS: A. S. DFT calculations: R. P. and M. C. L. Device fabrication, J–V, and IPCE: P. R. Visualization: A. S., S. N. and E. W.-G. D. Funding acquisition: E. W.-G. D. Supervision: S. N. and E. W.-G. D. Writing – original draft: A. S. Writing – review and editing: S. N. and E. W.-G. D.

Conflicts of interest

There are no conflicts to declare.

Acknowledgements

References

1 H. Min, D. Y. Lee, J. Kim, G. Kim, K. S. Lee, J. Kim, M. J. Paik, Y. K. Kim, K. S. Kim, M. G. Kim, T. J. Shin and S. I. Seok, *Nature*, 2021, **598**, 444–450.

2 NREL, *Best Research-Cell Efficiency Chart*, https://www.nrel.gov/pv/assets/pdfs/best-research-cell-efficiencies.pdf.

3 E. Aktas, N. Rajamanickam, J. Pascual, S. Hu, M. H. Aldamasy, D. Di Girolamo, W. Li, G. Nasti, E. Martínez-Ferrero, A. Wakamiya, E. Palomares and A. Abate, *Commun. Mater.*, 2022, **3**, 104.

4 L. Lanzetta, T. Webb, N. Zibouche, X. Liang, D. Ding, G. Min, R. J. E. Westbrook, B. Gaggio, T. J. Macdonald, M. S. Islam and S. A. Haque, *Nat. Commun.*, 2021, **12**, 2853.

5 A. Treglia, F. Ambrosio, S. Martani, G. Folpini, A. J. Barker, M. D. Albaqami, F. De Angelis, I. Poli and A. Petrozza, *Mater. Horiz.*, 2022, **9**, 1763–1773.

6 E. Jokar, C.-H. Chien, A. Fathi, M. Rameez, Y.-H. Chang and E. W.-G. Diau, *Energy Environ. Sci.*, 2018, **11**, 2353–2362.

7 J. You, M. Wang, C. Xu, Y. Yao, X. Zhao, D. Liu, J. Dong, P. Guo, G. Xu, C. Luo, Y. Zhong and Q. Song, *Sustainable Energy Fuels*, 2021, **5**, 2660–2667.

8 Y. Chen, K. Wang, H. Qi, Y. Zhang, T. Wang, Y. Tong and H. Wang, *ACS Appl. Mater. Interfaces*, 2022, **14**, 41086–41094.

9 Z. Zhu, X. Jiang, D. Yu, N. Yu, Z. Ning and Q. Mi, *ACS Energy Lett.*, 2022, **7**, 2079–2083.

10 E. W.-G. Diau, E. Jokar and M. Rameez, *ACS Energy Lett.*, 2019, **4**, 1930–1937.

11 F. Hao, C. C. Stoumpos, P. Guo, N. Zhou, T. J. Marks, R. P. H. Chang and M. G. Kanatzidis, *J. Am. Chem. Soc.*, 2015, **137**, 11445–11452.

12 X. Jiang, H. Li, Q. Zhou, Q. Wei, M. Wei, L. Jiang, Z. Wang, Z. Peng, F. Wang, Z. Zang, K. Xu, Y. Hou, S. Teale, W. Zhou, R. Si, X. Gao, E. H. Sargent and Z. Ning, *J. Am. Chem. Soc.*, 2021, **143**, 10970–10976.

13 X. Liu, T. Wu, J.-Y. Chen, X. Meng, X. He, T. Noda, H. Chen, X. Yang, H. Segawa, Y. Wang and L. Han, *Energy Environ. Sci.*, 2020, **13**, 2896–2902.

14 D. Song, S. Narra, M.-Y. Li, J.-S. Lin and E. W.-G. Diau, *ACS Energy Lett.*, 2021, **6**, 4179–4186.

This journal is © The Royal Society of Chemistry 2023

J. Mater. Chem. A, 2023, **11**, 21089–21098 | **21097**

15 X. Liu, T. Wu, C. Zhang, Y. Zhang, H. Segawa and L. Han, *Adv. Funct. Mater.*, 2021, **31**, 2106560.

16 E. Jokar, H.-S. Chuang, C.-H. Kuan, H.-P. Wu, C.-H. Hou, J.-J. Shyue and E. Wei-Guang Diau, *J. Phys. Chem. Lett.*, 2021, **12**, 10106–10111.

17 Z. Zhang, M. A. Kamarudin, A. K. Baranwal, L. Wang, G. Kapil, S. R. Sahamir, Y. Sanehira, M. Chen, Q. Shen and S. Hayase, *ACS Appl. Mater. Interfaces*, 2022, **14**, 36200–36208.

18 J.-T. Lin, T.-C. Chu, D.-G. Chen, Z.-X. Huang, H.-C. Chen, C.-S. Li, C.-I. Wu, P.-T. Chou, C.-W. Chiu and H. M. Chen, *ACS Appl. Energy Mater.*, 2021, **4**, 2041–2048.

19 Y. Xu, K.-J. Jiang, P. Wang, W.-M. Gu, G.-H. Yu, X. Zhou and Y. Song, *New J. Chem.*, 2022, **46**, 2259–2265.

20 W.-G. Choi, C.-G. Park, Y. Kim and T. Moon, *ACS Energy Lett.*, 2020, **5**, 3461–3467.

21 S. Shao, J. Liu, G. Portale, H.-H. Fang, G. R. Blake, G. H. Ten Brink, L. J. A. Koster and M. A. Loi, *Adv. Energy Mater.*, 2018, **8**, 1702019.

22 F. Wang, X. Jiang, H. Chen, Y. Shang, H. Liu, J. Wei, W. Zhou, H. He, W. Liu and Z. Ning, *Joule*, 2018, **2**, 2732–2743.

23 B. B. Yu, Z. Chen, Y. Zhu, Y. Wang, B. Han, G. Chen, X. Zhang, Z. Du and Z. He, *Adv. Mater.*, 2021, **33**, 2102055.

24 E. Jokar, P.-Y. Cheng, C.-Y. Lin, S. Narra, S. Shahbazi and E. Wei-Guang Diau, *ACS Energy Lett.*, 2021, **6**, 485–492.

25 S. Shao, M. Nijenhuis, J. Dong, S. Kahmann, G. H. Ten Brink, G. Portale and M. A. Loi, *J. Mater. Chem. A*, 2021, **9**, 10095–10103.

26 T. Wu, D. Cui, X. Liu, X. Meng, Y. Wang, T. Noda, H. Segawa, X. Yang, Y. Zhang and L. Han, *Sol. RRL*, 2020, **4**, 2000240.

27 C. Ran, J. Xi, W. Gao, F. Yuan, T. Lei, B. Jiao, X. Hou and Z. Wu, *ACS Energy Lett.*, 2018, **3**, 713–721.

28 D. Yu, Q. Wei, H. Li, J. Xie, X. Jiang, T. Pan, H. Wang, M. Pan, W. Zhou, W. Liu, P. C. Y. Chow and Z. Ning, *Angew. Chem.*, 2022, **61**, e202202346.

29 T. Elmelund, R. A. Scheidt, B. Seger and P. V. Kamat, *ACS Energy Lett.*, 2019, **4**, 1961–1969.

30 J. Cho, J. T. Dubose, A. N. T. Le and P. V. Kamat, *ACS Mater. Lett.*, 2020, **2**, 565–570.

31 M. Ghasemi, B. Guo, K. Darabi, T. Wang, K. Wang, C.-W. Huang, B. M. Lefler, L. Taussig, M. Chauhan, G. Baucom, T. Kim, E. D. Gomez, J. M. Atkin, S. Priya and A. Amassian, *Nat. Mater.*, 2023, **22**, 329–337.

32 C. Eames, J. M. Frost, P. R. F. Barnes, B. C. O'Regan, A. Walsh and M. S. Islam, *Nat. Commun.*, 2015, **6**, 7497.

33 G. Richardson, S. E. J. O'Kane, R. G. Niemann, T. A. Peltola, J. M. Foster, P. J. Cameron and A. B. Walker, *Energy Environ. Sci.*, 2016, **9**, 1476–1485.

34 Akriti, E. Shi, S. B. Shiring, J. Yang, C. L. Atencio-Martinez, B. Yuan, X. Hu, Y. Gao, B. P. Finkenauer, A. J. Pistone, Y. Yu, P. Liao, B. M. Savoie and L. Dou, *Nat. Nanotechnol.*, 2021, **16**, 584–591.

35 Q. Li, Y. Zheng, Z. Wei, J. Xie, C. Zou, X. Liu, D. Liu, Z. Zhou, H. G. Yang, S. Yang and Y. Hou, *Adv. Energy Mater.*, 2022, **12**, 2202982.

36 S. Narra, C.-Y. Lin, A. Seetharaman, E. Jokar and E. W.-G. Diau, *J. Phys. Chem. Lett.*, 2021, **12**, 12292–12299.

37 S. Narra, E. Jokar, O. Pearce, C.-Y. Lin, A. Fathi and E. W.-G. Diau, *J. Phys. Chem. Lett.*, 2020, **11**, 5699–5704.

38 D. Ghosh, D. Acharya, L. Zhou, W. Nie, O. V. Prezhdo, S. Tretiak and A. J. Neukirch, *J. Phys. Chem. Lett.*, 2019, **10**, 5000–5007.

39 B. Chen, J. Song, X. Dai, Y. Liu, P. N. Rudd, X. Hong and J. Huang, *Adv. Mater.*, 2019, **31**, 1902413.

40 L. A. Muscarella, E. M. Hutter, F. Wittmann, Y. W. Woo, Y.-K. Jung, L. Mcgovern, J. Versluis, A. Walsh, H. J. Bakker and B. Ehrler, *ACS Energy Lett.*, 2020, **5**, 3152–3158.

41 H. Tsai, R. Asadpour, J.-C. Blancon, C. C. Stoumpos, O. Durand, J. W. Strzalka, B. Chen, R. Verduzco, P. M. Ajayan, S. Tretiak, J. Even, M. A. Alam, M. G. Kanatzidis, W. Nie and A. D. Mohite, *Science*, 2018, **360**, 67–70.

42 J. Zhao, Y. Deng, H. Wei, X. Zheng, Z. Yu, Y. Shao, J. E. Shield and J. Huang, *Sci. Adv.*, 2017, **3**, eaao5616.

43 T. Yu, X. Mao, X. Xu, Z. Wang and R. Zhang, *Chem. Phys. Lett.*, 2021, **769**, 138411.

44 C. Zhou, H. Lin, Y. Tian, Z. Yuan, R. Clark, B. Chen, L. J. Van De Burgt, J. C. Wang, Y. Zhou, K. Hanson, Q. J. Meisner, J. Neu, T. Besara, T. Siegrist, E. Lambers, P. Djurovich and B. Ma, *Chem. Sci.*, 2018, **9**, 586–593.

45 H. Chen, S. Teale, B. Chen, Y. Hou, L. Grater, T. Zhu, K. Bertens, S. M. Park, H. R. Atapattu, Y. Gao, M. Wei, A. K. Johnston, Q. Zhou, K. Xu, D. Yu, C. Han, T. Cui, E. H. Jung, C. Zhou, W. Zhou, A. H. Proppe, S. Hoogland, F. Laquai, T. Filleter, K. R. Graham, Z. Ning and E. H. Sargent, *Nat. Photonics*, 2022, **16**, 352–358.

46 Y. Liao, H. Liu, W. Zhou, D. Yang, Y. Shang, Z. Shi, B. Li, X. Jiang, L. Zhang, L. N. Quan, R. Quintero-Bermudez, B. R. Sutherland, Q. Mi, E. H. Sargent and Z. Ning, *J. Am. Chem. Soc.*, 2017, **139**, 6693–6699.

21098 | *J. Mater. Chem. A*, 2023, **11**, 21089–21098

This journal is © The Royal Society of Chemistry 2023